

# Effect of initial conditions on interaction between a boundary layer and a wall-mounted finite-length-cylinder wake

H. F. Wang

State Key Laboratory of Coal Combustion, Huazhong University of Science and Technology, Wuhan, Hubei, People's Republic of China and Department of Mechanical Engineering, The Hong Kong Polytechnic University, Hung Hom, Kowloon, Hong Kong

Y. Zhou<sup>a)</sup>

Department of Mechanical Engineering, The Hong Kong Polytechnic University, Hung Hom, Kowloon, Hong Kong

C. K. Chan

Department of Applied Mathematics, The Hong Kong Polytechnic University, Hung Hom, Kowloon, Hong Kong

K. S. Lam

Department of Civil and Structural Engineering, The Hong Kong Polytechnic University, Hung Hom, Kowloon, Hong Kong

(Received 23 January 2006; accepted 9 May 2006; published online 21 June 2006)

The effects of initial conditions on interaction between a boundary layer over a flat plate and flow around a wall-mounted finite-length cylinder were experimentally investigated. A square cylinder with a characteristic width ( $d$ ) of 20 mm and a length of  $H=5d$  was vertically mounted on a horizontal flat plate. Three different boundary layers were investigated, their momentum thickness being  $0.07d$ ,  $0.13d$ , and  $0.245d$ , respectively, measured at the cylinder axis in the absence of the cylinder. All the experiments were carried out in a closed-loop water tunnel at a Reynolds numbers of 11 500 based on  $d$  and the free-stream velocity  $U_\infty$ . It is found that initial boundary layer conditions have a profound effect on the near wake, including the flow near the cylinder free end that is well beyond the boundary layer. With increasing boundary layer thickness, the base vortex is enhanced, inducing a stronger upwash flow from the cylinder base, which acts to weaken the downwash free-end shear layer and the tip vortex. Consequently, spanwise vortices gain strength near the free end but impair near the wall, causing the ratio of symmetrically to antisymmetrically arranged vortices to vary and subsequently the Reynolds stresses to increase significantly in magnitude near the free end but to decrease near the wall. © 2006 American Institute of Physics. [DOI: 10.1063/1.2212329]

## I. INTRODUCTION

The flow around a two-dimensional (2D) cylinder has been investigated extensively in the past because of its importance to practical engineering applications. Most of previous studies are concerned with cross flow over a nominally infinite 2D cylinder.<sup>1–3</sup> However, engineering problems are frequently associated with the structures of finite length with one free end, e.g., pollutant transport around high-rise buildings, plume behaviors behind stacks, aerodynamic forces on cooling towers or other structures, and heat transfer in electronic circuit boards. Flow around a wall-mounted finite-length cylinder is much more complicated than that behind a slender one. First, the finite length of the cylinder implies non-negligible end effects, enhancing the three dimensionality of the flow. Second, the wall boundary layer may possibly interact with the quasiperiodic flow around the cylinder, resulting in a highly complex flow structure.

A few investigations<sup>4–6</sup> have been conducted in the past

on the influence of aspect ratio, i.e., the ratio of cylinder length ( $H$ ) to characteristic width ( $d$ ), on the near wake. It has been established that, when  $H/d$  falls below a critical value, about 3–4, antisymmetric vortex shedding from a circular cylinder is suppressed and the near wake is dominated by tip vortices formed by a downwash shear layer separated from the free end; with  $H/d$  exceeding the critical value, Kármán vortices occur for most of span except near the free end. For a finite-length square cylinder, the critical  $H/d$  was found to be about 2<sup>7</sup>. This critical value is dependent on the incoming flow turbulence intensity, boundary layer thickness, and other factors.<sup>5</sup>

The free-end downwash shear layer plays an important role in the formation of the near wake.<sup>6,8</sup> For a short obstacle, say  $H/d \leq 3-4$ , the free-end shear layer reattaches the wall.<sup>4,6</sup> For instance, Hunt *et al.*<sup>9</sup> and Hussein and Martinuzzi<sup>10</sup> observed reattachment at about  $2d$  downstream of a surface-mounted cube ( $H/d=1$ ). A recent large eddy simulation<sup>11</sup> unveiled an arch-type vortex around a wall-mounted finite-length circular cylinder with  $H/d=2.5$ , as observed for a wall-mounted cube.<sup>10</sup> As  $H/d$  exceeds 3–4, the

<sup>a)</sup> Author to whom correspondence should be addressed. Electronic mail: mmyzhou@polyu.edu.hk

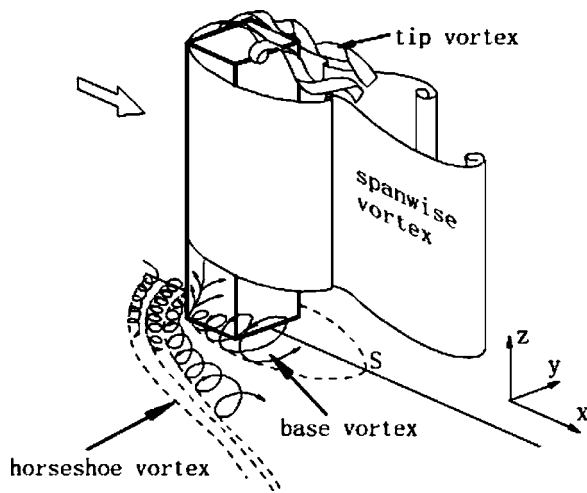


FIG. 1. Flow structures around wall-mounted finite-length square prism (Ref. 13).

downwash free-end shear layer will be confined near the free end. Based on flow visualization, Etzold and Fiedler<sup>4</sup> and Kawamura *et al.*<sup>5</sup> argued that the spanwise shear layer of a finite-length circular cylinder was oblique near the free end, moving upwards initially and then downwards with the downwash free-end shear layer, forming a pair of streamwise vortices, i.e., tip vortices. Etzold and Fiedler<sup>4</sup> and Sumner *et al.*<sup>12</sup> observed one pair of streamwise vortices near the cylinder base, which induced an upward flow. The vortices, referred to as the base vortices, were opposite in sense to the tip vortices near the free end, as illustrated schematically in Fig. 1 for a finite-length prism with  $H/d$  exceeding the critical value.<sup>13</sup>

For a wall-mounted finite-length cylinder, the initial condition of the boundary layer may have a profound impact on the near wake. The initial conditions have been found to influence a turbulent plane wake even far downstream.<sup>14–16</sup> Most of previous investigations of a finite-length-cylinder wake were conducted either in a uniform incoming flow<sup>17</sup> or with a very thin boundary layer compared with the cylinder height.<sup>6,8</sup> Sakamoto and Arie<sup>7</sup> obtained an empirical correlation between the Strouhal number and  $H/\delta$  ( $\delta$  is the boundary layer disturbance thickness) in their investigation of vortex shedding from a finite-length square and a circular cylinder placed in a fully developed turbulent boundary layer tripped by a rod fixed at the entrance of the test section. Recently, Park and Lee<sup>18</sup> investigated experimentally the flow structure around a finite-length circular cylinder ( $H/d = 6$ ) immersed in a boundary layer. Their flow visualization suggested that the free-end shear layer moved down more rapidly in the presence of a turbulent boundary layer than in a uniform incoming flow. They further suggested that the downwash shear layer had little influence upon vortices shed from the half of the cylinder near the base.

In spite of previous investigations, the effect of the initial conditions of the boundary layer on the near wake has not been thoroughly understood. In engineering applications, the boundary layer conditions can be very different. This work aims to investigate this effect on the near wake of a

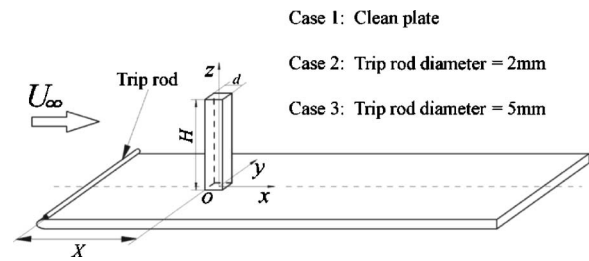


FIG. 2. Experimental setup and the definition of the coordinate system.

wall-mounted finite-length square cylinder. The aspect ratio ( $H/d$ ) of the square cylinder was chosen to be 5 in view of the fact that spanwise vortices may not exist below the critical  $H/d$  and the wall boundary layer may be less important for a large  $H/d$ . Three boundary layers of different thickness were examined. The flow was measured mainly using particle image velocimeter (PIV). Based on the measurements, a comparison is made in detail in the three-dimensional (3D) flow structure, along with the mean and Reynolds stresses, between different boundary conditions.

## II. EXPERIMENTAL DETAILS

Experiments were performed in a closed-loop water tunnel with a 2.4-m-long test section, which has a cross section of 0.3 m wide and 0.6 m high. A 1-m-long and 10-mm-thick flat plate of the same width as the test section was horizontally installed, its upper surface being 0.45 m from the upper wall of the test section. A square cylinder of  $d=20$  mm and  $H=100$  mm was mounted at the mid of the plate, 0.25 m downstream of the leading edge. The blockage ratio was 0.028. See Fig. 2 for the schematic of the experimental setup and the definition of the coordinate system.

The incoming flow velocity  $U_\infty$  was  $0.58 \text{ ms}^{-1}$ , corresponding to a Reynolds number  $Re_d (\equiv U_\infty d / \nu, \text{ where } \nu \text{ is the kinematic viscosity of fluid}) = 11\,540$  and  $Re_X (\equiv U_\infty X / \nu, \text{ where } X \text{ is the streamwise distance from the leading edge}) = 1.44 \times 10^5$ . At this  $U_\infty$ , the free-stream longitudinal turbulent intensity was about 1.2%, and the nonuniformity of the streamwise velocity was less than 0.1%. Three different initial conditions of the boundary layer were investigated. Case 1: a clean plate was used to generate a laminar boundary layer ( $Re_X = 1.44 \times 10^5 < 5 \times 10^5$ ); case 2: a tripping rod of 2 mm in diameter was placed at the leading edge of the plate; case 3: the diameter of the tripping rod was 5 mm. Figure 3 presents the time-averaged and the rms streamwise velocities,  $\overline{u}$  and  $u_{\text{rms}}^*$ , of the three different boundary layers measured using a two-component laser Doppler anemometer (LDA) along the cylinder axis in the absence of the cylinder. See Wang *et al.*<sup>19</sup> for the details of the LDA system. In this paper, an asterisk denotes normalization by  $U_\infty$  and/or  $d$ . It is evident that the thickness of the tripped boundary layer grew considerably, accompanied by greatly enhanced  $u_{\text{rms}}^*$ , suggesting a turbulent boundary layer. The major characteristic properties of the boundary layers are summarized in Table I.

A DANTEC standard PIV2100 system was used to measure the flow field. The flow was seeded by  $20 \mu\text{m}$  polyamide particles with a density of  $1.03 \text{ g/cm}^3$ , approximately

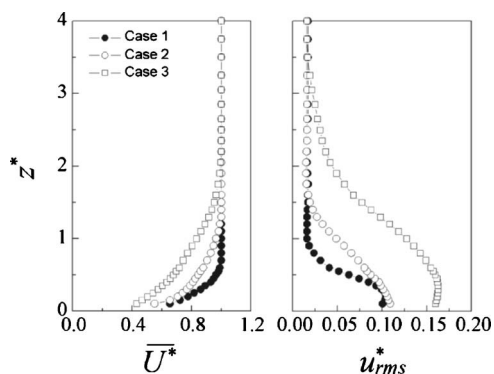


FIG. 3. Distributions of the streamwise mean and rms velocities measured at  $x^*=0$ , where the prism was mounted. Measurements were performed in the absence of the prism.

the same as the water. Flow illumination was provided by two Newwave standard pulse laser sources of a 532 nm wavelength, each with a maximum energy output of 120 mJ/pulse. Each pulse lasted for 0.01  $\mu$ s. An optical filter was used to allow only the green wavelength (532 nm) of the laser source to pass. Particle images were taken using one CCD camera (HiSense type 13, gain  $\times 4$ , double frames,  $1280 \times 1024$  pixels). Synchronization between image taking and flow illumination was provided by the Dantec FlowMap Processor (PIV2001 type). In order to evaluate the three dimensionality of the near wake, PIV measurements were performed in the  $x$ - $z$  plane at  $y/d=0$  and the  $x$ - $y$  plane at  $z/d=1, 2.5$ , and 4, respectively. The lateral and spanwise image magnifications were identical for each measurement, ranging from 113 to 106  $\mu$ m/pixel. The interval between two successive pulses was 600  $\mu$ s for all the measurements. Thus, a particle would travel only about 0.35 mm (0.018 $d$ ) at  $U_\infty=0.58$  ms $^{-1}$ . The interrogation area consisted of  $64 \times 64$  pixels ( $\approx 0.34d$ ) with a 50% overlap in both directions. Accordingly, the in-plane velocity vector field included  $39 \times 31$  vectors, which produced the same number of vorticity data. The spatial resolution for vorticity estimate was about 0.17 $d$ . Due to a limited spatial resolution, the velocity derivatives in the vorticity components are expected to be underestimated. This underestimate should not to a great extent adversely affect the present investigation since the small-scale turbulent structures are not of concern here. Five hundred images were captured, based on which the mean and rms velocities and Reynolds shear stress were calculated. It has been confirmed that the maximum scattering is within

2% in the mean or fluctuating velocities if averaging is performed between 400 and 500 PIV images.

### III. FLOW STRUCTURE IN THE $x$ - $z$ PLANE

#### A. Averaged flow structure

Figure 4 presents time-averaged sectional streamlines, viewed on a fixed reference frame, and the corresponding vorticity contours in the central plane ( $y^*=0$ ). The reverse flow region, i.e.,  $\overline{U^*} \leq 0$ , is denoted by a thick solid line in the figure. For all the three cases, the free-end shear layer rolls down towards the wall. With  $H/d=5$  exceeding the critical value (about 2 for a square cylinder<sup>7</sup>), the free-end shear layer does not reattach on the wall [Figs. 4(a), 4(c), and 4(e)]. The rolling down free-end shear layer within the reverse flow region appears retreating gradually with the increasing boundary layer thickness. The corresponding vorticity contours [Figs. 4(b), 4(d), and 4(f)] also shrink in size. This change implies an altered lifting force near the cylinder free-end and pressure distribution on the wall, which balance the momentum of the downwash free-end shear layer.<sup>4</sup>

An upwash flow originating from the cylinder base near the wall is evident, and appears clashing with the downwash free-end shear layer, acting to prevent the downwash flow from reattaching on the wall. This upwash flow is enhanced as the boundary layer grows thicker. The upwash flow cannot be ascribed to the horseshoe vortex, characterized by a rollup motion in front of the obstacle, wrapping around from both sides and trailing off behind. The horseshoe vortex tends to drive flow downwards inside its vertical tails.<sup>10,20</sup> Etzold and Fiedler<sup>4</sup> suggested the presence of one pair of streamwise vortices near the cylinder base, referred to as the base vortex hereinafter, which rotate oppositely to the tip vortex. Both the base and tip vortices induce flow towards the cylinder midspan. The enhanced upwash flow with growing boundary layer thickness may suggest the strengthened base vortex.

Figure 5 compares the reverse flow region of the three cases, along with the data of a 2D square cylinder measured by Lyn *et al.*<sup>21</sup> The symbols “ $\otimes$ ” and “ $\times$ ” denote the saddle and focus points<sup>22</sup> observed in Fig. 4, respectively. The streamwise extent of the reverse flow region is significantly enlarged compared with that of the 2D cylinder. In case 1, when the boundary layer effect is limited, the reverse flow region is almost independent of  $z^*$  for  $z^* \leq 2.5$ . The observation is similar to experimental results of Etzold and Fiedler<sup>4</sup> and Okamoto and Sunabashiri<sup>6</sup> for a finite-length circular cylinder ( $H/d=6$ ) immersed in a thin boundary layer. The

TABLE I. Characteristic properties of the boundary layer.

	Diameter of trip wire (mm)	Disturbance thickness $\delta$ (mm)	Displacement thickness $\delta_1$ (mm)	Momentum thickness $\theta$ (mm)	Friction velocity $u_\tau/U_\infty$	Shape parameter $\delta_1/\theta$
Case 1	0	10.2	2.5	1.4	0.051	1.8
Case 2	2	20.3	4.2	2.6	0.047	1.6
Case 3	5	38.0	8.7	4.9	0.043	1.8

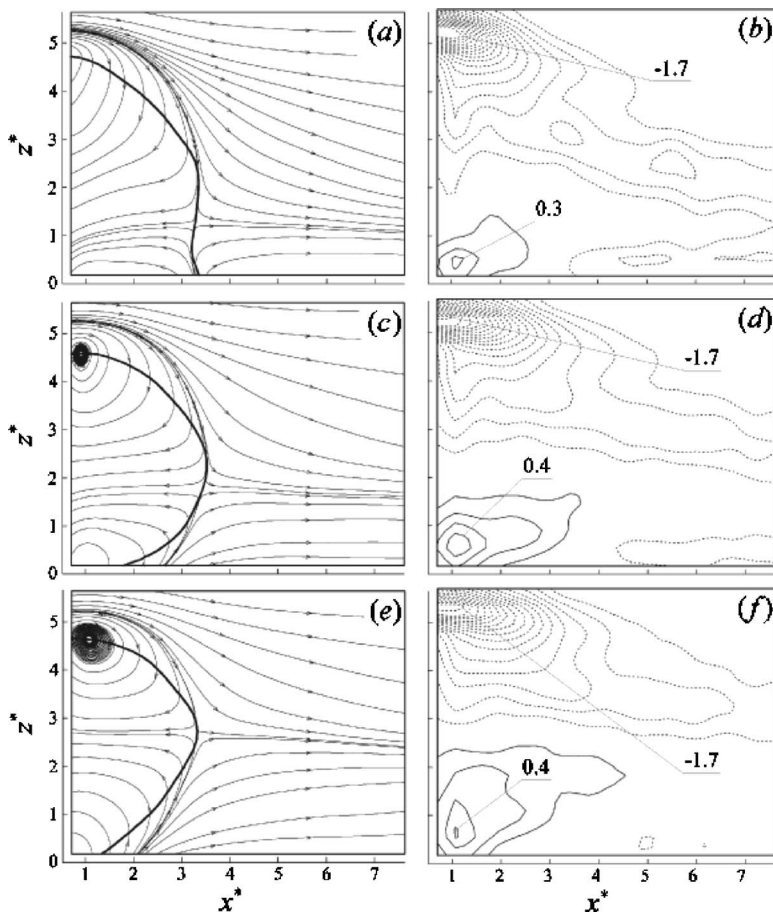


FIG. 4. Averaged sectional streamlines (left) in the  $x$ - $z$  plane at  $y^*=0$ , viewed on a reference frame fixed on the wall, and the corresponding contours of lateral vorticity  $w_y^*$  (right), contour increment=0.2. (a), (b) Case 1, (c), (d) case 2, (e), (f) case 3. The thick solid line indicates the reverse flow region.

saddle point, which can be considered to be the dividing point of downwash and the upwash flow (Fig. 4), moves upwards gradually with growing boundary layer thickness from case 1 to case 3, indicating the growing upwash flow. The growing boundary layer thickness results in a decrease of the size of the reverse flow region in the lower part but an increase in the upper.

**B. Mean velocity and Reynolds stresses**

Figures 6–10 present the spanwise distributions of the averaged streamwise and spanwise velocities and Reynolds

stresses, i.e.,  $\overline{U^*}$ ,  $\overline{W^*}$ ,  $\overline{u^{*2}}$ ,  $\overline{w^{*2}}$ ,  $\overline{u^*w^*}$  at  $y^*=0$  for various downstream locations. In this paper, unless otherwise stated, the overbar indicates averaging based on 500 instantaneous PIV images. For all the three cases,  $\overline{U^*}$  (Fig. 6) depends strongly on  $z^*$  because of the end effects and is negative along most of the span for  $x^*<4$ . At  $x^*=1$ ,  $\overline{U^*}$  [Fig. 6(a)] displays a similar distribution for different cases except near the midspan of the cylinder, where the tripped boundary layers contribute to a more significant reverse flow. The effects of the initial conditions on  $\overline{U^*}$  becomes more evident near the wall at  $x^*=2$  [Fig. 6(b)];  $\overline{U^*}$  is less negative with the boundary layer tripped. Interestingly, at  $x^*\geq 2$ ,  $\overline{U^*}$  is appreciably smaller above the midspan of the cylinder, which is outside the boundary layer, with tripping than without [Figs.

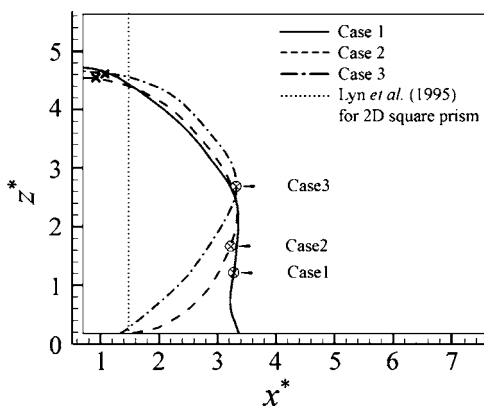


FIG. 5. Averaged reverse flow region for the three tested cases. The saddle and foci points in Fig. 4 are denoted by “ $\otimes$ ” and “ $\times$ ”, respectively.

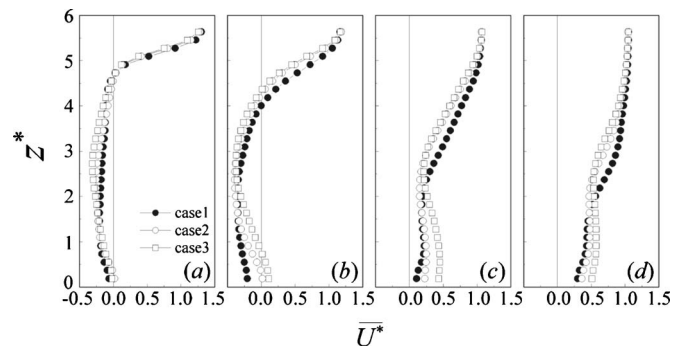


FIG. 6. Spanwise variation of  $\overline{U^*}$ : (a)  $x^*=1$ , (b)  $x^*=2$ , (c)  $x^*=4$ , (d)  $x^*=6$ .

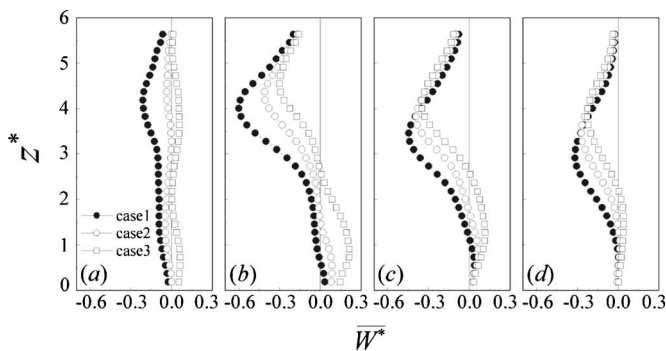


FIG. 7. Spanwise variation of  $\overline{W^*}$ : (a)  $x^*=1$ , (b)  $x^*=2$ , (c)  $x^*=4$ , (d)  $x^*=6$ .

6(b)–6(d)]. It may be concluded that the increasing boundary layer thickness leads to an increase in  $\overline{U^*}$  for  $z^* \leq 2$  but a decrease for  $z^* \geq 2$ .

Averaged spanwise velocity  $\overline{W^*}$  (Fig. 7) exhibits a dependence on the initial conditions stronger than  $\overline{U^*}$ . At  $x^*=1$  [Fig. 7(a)],  $\overline{W^*}$  for case 1 is negative along the entire span, especially near the free end, as a result of the downwash free-end shear layer [Fig. 4(a)]. As the boundary layer becomes thicker,  $\overline{W^*}$  is less negative in case 2 and almost all positive in case 3. This is because a thick boundary layer acts to enhance the upwash flow from the wall, which acts to restrain the downwash flow [Figs. 4(c)–4(e)]. At  $x^*=2$  and 4,  $\overline{W^*}$  remains negative for case 1 except very close to the wall, that is, the downwash flow continues to be predominant along the entire span, which is consistent with sectional streamlines (Fig. 4). On the other hand, the enhancement of the upwash flow near the wall and the restrained downwash flow above the mid span is more evident [Figs. 7(b) and 7(c)]. However, at  $x^*=6$ , the positive  $\overline{W^*}$  disappears near the wall, suggesting the absence of the upwash flow, whereas the negative  $\overline{W^*}$  above the midspan, albeit less pronounced, still persists. The observation is attributed to the fact that the base vortex decays much more quickly than the tip vortex.<sup>12,13</sup> Note that the negative peak shifts towards the free end with increasing boundary layer thickness [Figs. 7(b)–7(d)] because the downwash free-end shear layer is pushed up by the enhanced upwash flow.

The spanwise distributions of  $\overline{u^{*2}}$  (Fig. 8) and  $\overline{w^{*2}}$  (Fig. 9) at  $y^*=0$  display a great difference at  $x^*>2$  but qualitative similarity for  $x^*\leq 2$ . A peak is evident near  $z^*=5$  in  $\overline{u^{*2}}$  up to

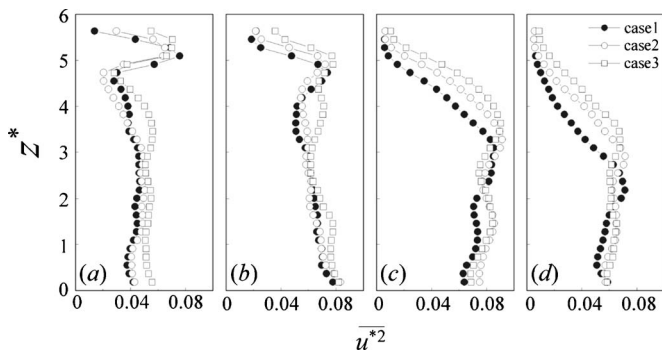


FIG. 8. Spanwise variation of  $\overline{u^{*2}}$ : (a)  $x^*=1$ , (b)  $x^*=2$ , (c)  $x^*=4$ , (d)  $x^*=6$ .

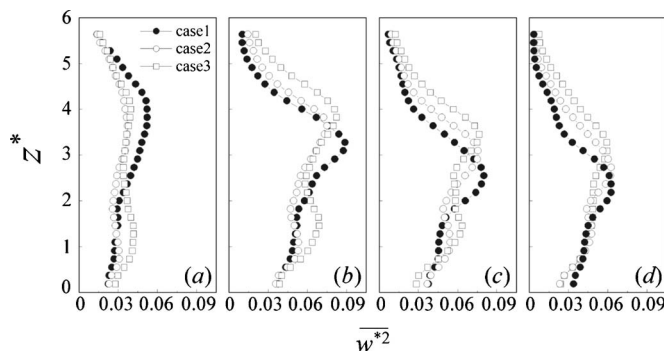


FIG. 9. Spanwise variation of  $\overline{w^{*2}}$ : (a)  $x^*=1$ , (b)  $x^*=2$ , (c)  $x^*=4$ , (d)  $x^*=6$ .

$x^*=2$ , apparently connected to the free-end shear layer. Interestingly, the increasing boundary layer thickness affects not only  $\overline{u^{*2}}$  near the wall but also  $\overline{u^{*2}}$  well beyond the boundary layer, which is more evident for  $x^*\geq 4$ . With the increasing boundary layer,  $\overline{w^{*2}}$  at  $x^*=1$  is suppressed at  $z^*\geq 2$  but enhanced at  $z^*\leq 2$ , especially for case 3 [Fig. 9(a)]. At  $x^*=2$  and 4,  $\overline{w^{*2}}$  [Figs. 9(b) and 9(c)] displays one peak above the mid span for all the three cases; with the boundary layer tripped, a hump occurs at  $z^*\approx 1$  in  $\overline{w^{*2}}$ . The former is ascribed to the rolling down free-end shear layer and shifts towards the free end under the influence of the enhanced upwash flow for a thicker boundary layer. The latter is attributed to the upwash flow and invisible at  $x^*=6$  [Fig. 9(d)] due to the disappearance of the base vortex.

The Reynold shear stress  $\overline{u^*w^*}$  (Fig. 10) is rather small in magnitude. In general,  $\overline{u^*w^*}$  is negative at  $z^*\geq 2.5$  because the downwash flow ( $w<0$ ) is associated with the high momentum fluid ( $u>0$ ) entrained from the free stream. On the other hand,  $\overline{u^*w^*}$  tends to be positive at  $z^*\leq 2.5$ , particularly for  $x^*\geq 2$ , probably because the upwash flow ( $w>0$ ) is associated with relatively high momentum fluid, i.e.,  $u>0$  (see Fig. 6). This stress  $\overline{u^*w^*}$  differs significantly along the entire span between the different cases, in particular, at  $x^*\leq 4$ , indicating that the boundary layer thickness has a profound influence on the momentum transport.

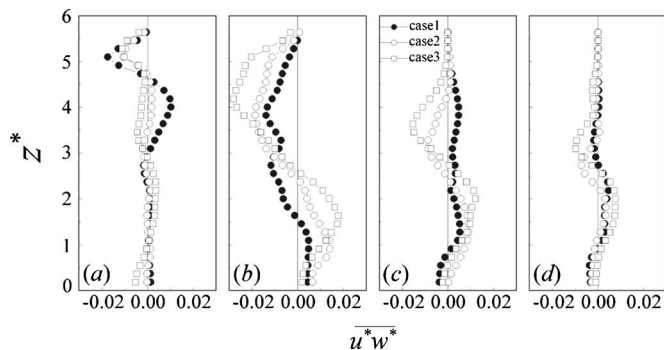
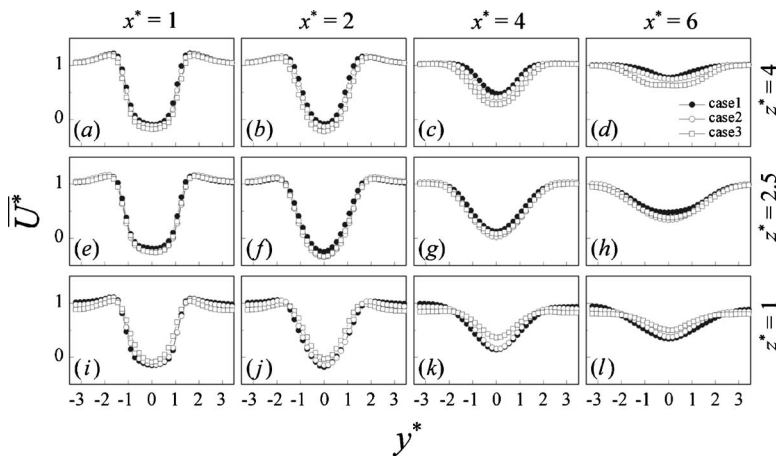


FIG. 10. Spanwise variation of Reynolds shear stress  $\overline{u^*w^*}$ : (a)  $x^*=1$ , (b)  $x^*=2$ , (c)  $x^*=4$ , (d)  $x^*=6$ .

FIG. 11. Lateral distribution of  $\overline{U}^*$ .

#### IV. SPANWISE FLOW STRUCTURE

##### A. Mean velocities and Reynolds stresses in the $x$ - $y$ plane

Figures 11–15 present the lateral distributions of  $\overline{U}^*$ ,  $\overline{V}^*$ ,  $\overline{u^{*2}}$ ,  $\overline{v^{*2}}$ , and  $\overline{u^*v^*}$  measured at  $z^*=1, 2.5$ , and 4 and  $x^*=1, 2, 4$ , and 6, respectively. A number of observations can be made.

First, the effect of the boundary layer on  $\overline{U}^*$  (Fig. 11) seems to be limited at  $x^*=1$  and 2, but appreciable further downstream at  $x^*=4$  and 6, especially near the free-end [Figs. 11(c) and 11(d)] and the wall [Figs. 11(k) and 11(l)]. In general,  $\overline{U}^*$  near the centerline is increased at  $z^*=1$ , while that at  $z^*=4$  diminishes gradually, with increasing boundary layer thickness. As noted in Sec. III A, a thicker boundary layer enhances the upwash flow, which suppresses the downwash free-end shear layer. The upwash and downwash flows are essentially associated with the counter-rotating base and the tip vortices,<sup>4</sup> respectively. Both types of vortices may act to entrain high-speed fluid relatively far away from the cylinder into the wake, as illustrated in Fig. 1. Consequently, the enhanced base vortex causes an increase in  $\overline{U}^*$  at  $z^*=1$ , and the weakened tip vortex is associated with a decrease in  $\overline{U}^*$  at  $z^*=4$ .

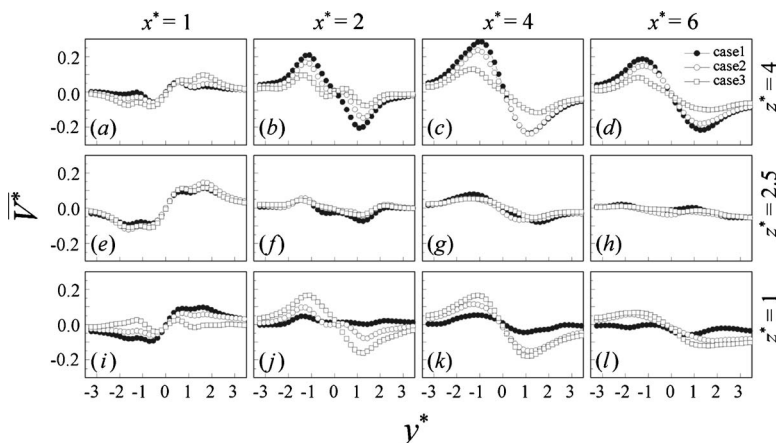
Second,  $\overline{V}^*$  at  $x^*=1$  [Figs. 12(a), 12(e), and 12(i)] shows a sign opposite to that at other downstream stations for all cases [Figs. 12(b)–12(d), 12(f)–12(h), and 12(j)–12(l)]. This

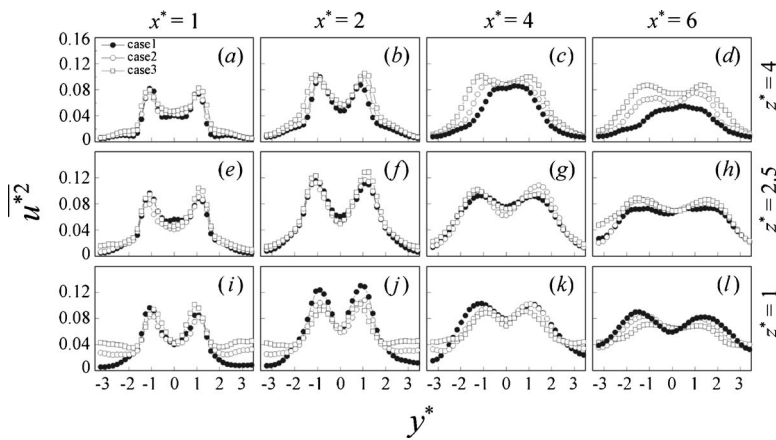
is simply because  $\overline{V}^*$  changes sign at the streamwise position, where the maximum lateral width of the reverse flow region occurs, as illustrated in Fig. 16.

Third,  $\overline{V}^*$  decays rapidly at  $z^*=2.5$ , similarly to the observations of Lyn *et al.*<sup>21</sup> and Saha *et al.*<sup>23</sup> in the wake of a 2D square cylinder, which showed a rapid decay in  $\overline{V}^*$  with increasing  $x^*$ , almost to zero at  $x^*=4$ . The similarity is not surprising since spanwise vortices are predominant near the midspan. However,  $\overline{V}^*$  persists further downstream at  $z^*=1$  and 4, which is expected because the vortex formation mechanisms are totally different between spanwise, tip, and base vortices.

Fourth, the boundary layer condition has a very significant effect on  $\overline{V}^*$  near the free end as well as near the wall. Presumably,  $\overline{V}^*$  is largely induced by the tip vortex associated with the downwash flow or the base vortex associated with the upwash flow. The enhanced base vortex in cases 2 and 3 will naturally cause  $\overline{V}^*$  larger in magnitude at  $z^*=1$ . On the other hand, the impaired tip vortex in the two cases is responsible for the retreating  $\overline{V}^*$  at  $z^*=4$ .

Fifth, excluding  $x^*=1$  (where  $\overline{V}^*$  shows a sign opposite to that at other downstream stations),  $\overline{V}^*$  [Figs. 12(a)–12(d)] reaches its maximum at  $x^*=4$  for all cases. Coincidentally, the maximum  $\overline{u^{*2}}$ ,  $\overline{v^{*2}}$ , and  $\overline{u^*v^*}$  [Figs. 13–15] all occur at  $x^*=4$ . It is well known that the formation length of spanwise vortices is defined at the maximum centerline  $\overline{u^{*2}}$  in a plane

FIG. 12. Lateral distribution of  $\overline{V}^*$ .

FIG. 13. Lateral distribution of  $\overline{u^{*2}}$ .

wake.<sup>24</sup> The occurrence of the maximum centerline  $\overline{u^{*2}}$ ,  $\overline{v^{*2}}$ , and  $\overline{u^*v^*}$  may signal the formation length of present spanwise vortices.

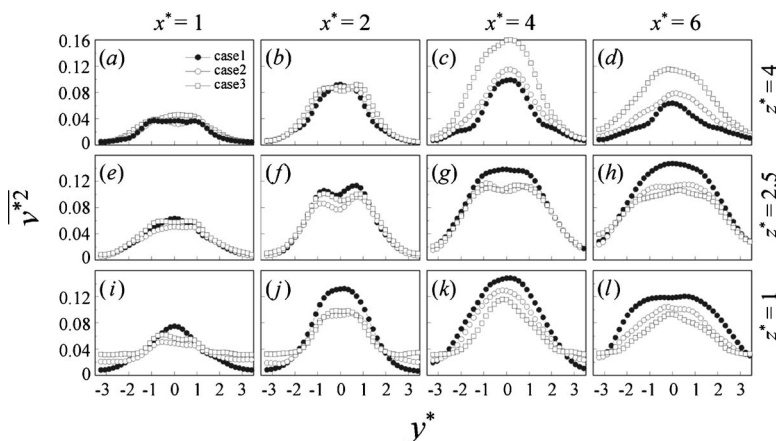
Sixth,  $\overline{u^{*2}}$  displays a twin-peak distribution for all cases, indicating the occurrence of two rows of vortices. In contrast,  $\overline{v^{*2}}$  shows a single peak and  $\overline{u^*v^*}$  is antisymmetric about  $y^*=0$ . The two peaks in  $\overline{u^{*2}}$  occur at  $y^* \approx \pm 1$  for  $x^*=1$  and 2. With a further increase in  $x^*$ , the peaks become broad and move further away from the centerline. In comparison, the two peaks of  $\overline{u^{*2}}$  behind a 2D square cylinder occur at  $y^* \approx \pm 0.6$  for  $x^*=1.5$ .<sup>21,23</sup> This suggests that the wake width grows in a finite-length-cylinder wake, which is attributed to the influence of the tip and base vortices. Note that  $\overline{u^{*2}}$  and  $\overline{v^{*2}}$  at  $z^*=1$  is considerably greater at  $|y^*| > 1.5$  in cases 2 and 3 than in case 1 [Figs. 13(i)–13(k)], apparently due to the higher turbulent intensity of the boundary layers.

Finally,  $\overline{u^{*2}}$ ,  $\overline{v^{*2}}$ , and  $\overline{u^*v^*}$  [Figs. 13–15] exhibit appreciable dependence on the boundary conditions, not only near the wall but also near the free end. With increasing boundary layer thickness, they are enhanced near the free end but suppressed near the wall. The observation is again connected to impaired spanwise vortices near the wall under the influence of the enhanced base vortex and to strengthened spanwise vortices near the free end due to the weakened tip vortex.

## B. Flow structure around the cylinder in the $x$ - $y$ plane

Since the flow structure is highly 3D, varying greatly along the cylinder span, the measurements were conducted at  $z^*=1, 2.5$ , and 4 for each case so that the vortex behavior may be examined at the midspan, near the free end and the wall. Figure 17 presents the  $\overline{\omega_z^*}$  contours. The same lowest  $\overline{\omega_z^*}$  in magnitude and contour increment are used for the purpose of comparison. The reverse flow region determined from sectional streamlines is marked by a thick solid line to facilitate data interpretation. There is a marked difference in the size of the reverse flow region; this size is the largest in the midspan, but shrinks near the wall apparently under the effect of the base vortex. This size is smallest near the free end. The flow near the free end is dominated by the rolling down free-end shear layer, which tends to suppress alternate shedding of spanwise vortices.<sup>25</sup> The small reverse flow region near the free end conforms to the observation in a finite-length circular-cylinder wake.<sup>4,6</sup> The variation in the longitudinal size of the reverse flow region is also internally consistent with that shown in the  $x$ - $z$  plane [Figs. 4(a), 4(c), and 4(e)].

At  $z^*=4$  the size of the same level contour increases progressively from case 1 to case 3, while the highest level

FIG. 14. Lateral distribution of  $\overline{v^{*2}}$ .

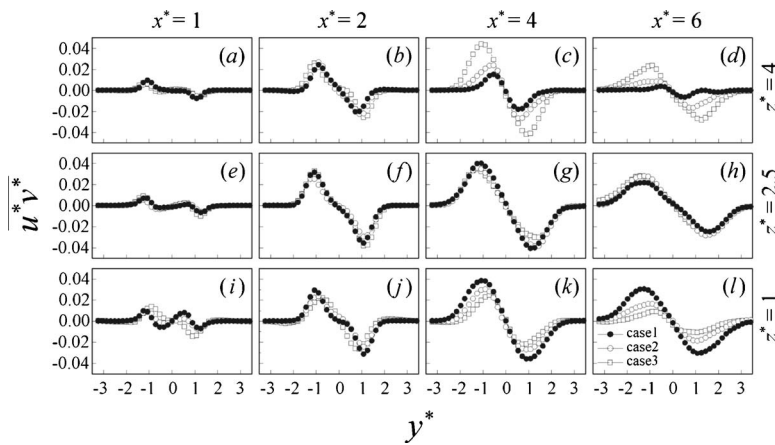


FIG. 15. Lateral distribution of the Reynolds shear stress  $u^*v^*$ .

remains unchanged. A similar observation was made at  $z^* = 2.5$ , though the same level contour size grows to a lesser extent. At  $z^* = 1$ , however, the same level contour is downsized considerably from case 1 to case 3; for example, the streamwise extent of the contour of  $\omega_z^* = \pm 0.3$  shrinks by almost one third. Furthermore, the highest concentration of  $\omega_z^*$  drops by one third. This marked variation reflects an important change in the flow structure near the wall: alternately formed spanwise vortices may dominate in case 1; however, the dominance is gradually taken over by the base vortex with the increasing boundary layer. The observation further suggests that the base vortex is probably characterized by a considerably smaller vorticity concentration and size than the spanwise vortex.

Based on their flow visualization at  $Re = 270 - 730$ , Sakamoto and Arie<sup>7</sup> classified vortices in the near wake of a wall-mounted finite-length square cylinder into two major types as illustrated in Fig. 18: one was Kármán-type vortices, referred to as T1, which occurred antisymmetrically about  $y^* = 0$ ; the other was the so-called arch-type vortices arranged symmetrically, referred to as T2. They suggested a predominance by the latter in the near wake of a square cylinder of  $H/d \lesssim 2$ , but by the former if  $H/d \gtrsim 2$ . At  $H/d \approx 2$ , both types of vortices were observed intermittently. Both types of vortices were presently observed at all spanwise locations, in spite of the present  $H/d$  larger than the critical value proposed by Sakamoto and Arie,<sup>7</sup> as illustrated in Fig. 19 (for case 1). Similar observations were made for cases 2 and 3.

It could be interesting to examine how the boundary layer conditions would affect the occurrence of the two types of vortices. To this end, the vortex center has to be first identified from the PIV data. A wide variety of methods have been used for detecting the organized motion in a turbulent flow, such as vorticity technique,<sup>26,27</sup> critical-point technique,<sup>22,28</sup> and phase-averaging technique.<sup>29,30</sup> Hunt *et al.*<sup>31</sup> proposed a  $Q$ -criterion method to detect the vortex center, which is essentially similar to the critical-point technique.<sup>22,28</sup> This method was successfully used by Dubief and Delcayre<sup>32</sup> to identify the vortex structure in isotropic turbulence, backward-facing step and channel flows, and is presently used. Readers may refer to Hunt *et al.*<sup>31</sup> and Jeong and Hussain<sup>33</sup> for a detailed description of the technique. Briefly, the criterion  $Q$  is defined as

$$Q = \frac{1}{2}(r_{ij}r_{ij} - s_{ij}s_{ij}), \tag{1}$$

where  $s_{ij}$  and  $r_{ij}$  are the symmetrical strain tensor and skew-symmetrical rotation tensor given by

$$s_{ij} = \frac{1}{2} \left( \frac{\partial u_i}{\partial x_j} + \frac{\partial u_j}{\partial x_i} \right), \tag{2}$$

$$r_{ij} = \frac{1}{2} \left( \frac{\partial u_i}{\partial x_j} - \frac{\partial u_j}{\partial x_i} \right), \tag{3}$$

where  $i, j = 1, 2, \text{ and } 3$ ;  $u_1, u_2, \text{ and } u_3$  are the velocity components along the  $x_1, x_2, \text{ and } x_3$  directions of the Cartesian coordinate system, respectively. The 2D velocity gradient tensor was presently used since the PIV-measured velocity data are 2D.  $Q$  is calculated from the velocity data using (1)-(3). A vortex is detected once the following condition is satisfied:

$$Q \geq kQ_m, \tag{4}$$

where  $Q_m$  is the maximum  $Q$  in the velocity field captured by each PIV image, and  $k$  is a threshold, which is chosen to be 0.7 in the present context. The determination of this threshold is based on visually comparing detected vortices with the contours of PIV-measured  $\omega_z$  so that the small-scale vortical structures, e.g., the structure at  $(x^*, y^*) = (4.6, 1.5)$  in Fig 19(a) and the one at  $(x^*, y^*) = (5.7, -1.3)$  in Fig 19(d), will not be detected, which are not of interest here. The location of the local maximum  $Q$ , which satisfies (4), is identified with the vortex center. It has been verified that the detections agree quite well with the plotted vorticity contours, as illus-

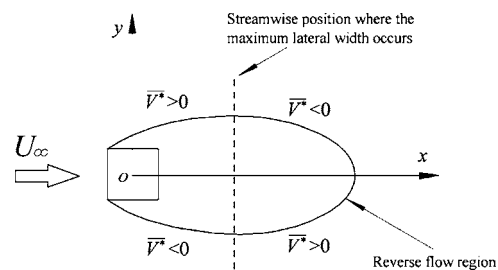


FIG. 16. The sign of time-averaged lateral velocity.

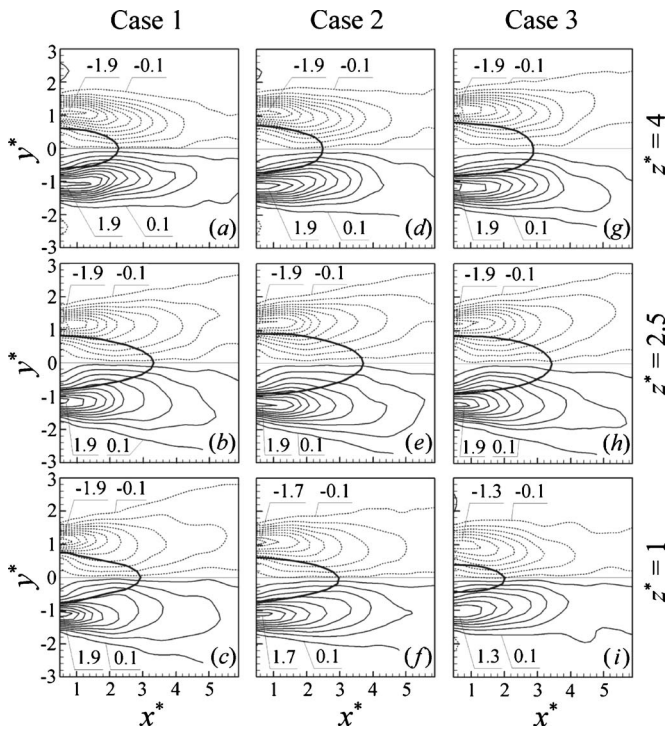


FIG. 17. Contours of averaged vorticity  $\bar{\omega}_z^*$  (contour increment=0.2).

trated in Fig. 19, where the detected vortex centers are marked by “×.”

In order to determine whether vortex shedding is anti-symmetrical or symmetrical, the center-to-center streamwise spacing between two vortices of the same sign is equally divided into four regions, i.e., I, II, III, and IV (Fig. 20). Vortices are considered to be anti-symmetrical if the center of an opposite-sign vortex in the other row falls in regions II or III, and symmetrical otherwise.

Figure 21 displays the probabilities of anti-symmetrical vortex shedding at various spanwise positions. For case 1, anti-symmetrical vortex shedding accounts for 84.1% at  $z^*=1$ , that is, the near wake close to the wall is dominated by alternating vortex shedding. However, at  $z^*=4$ , 80.5% (100%-19.5%) of vortex shedding is symmetrical, the wake near the free end being dominated by symmetrical vortex shedding. The result is consistent with the report by Okamoto and Sunabashiri,<sup>6</sup> who examined the variation of vortex shedding types along the spanwise direction for a finite-length circular cylinder with  $H/d=7$  ( $Re=1060$ ) and suggested that anti-symmetrical vortex shedding disappear at  $0.5d$  from the free end. Nevertheless, the present result indicates the survival of about 20% of anti-symmetrical vortex shedding at  $1d$  away from the free end of the square cylinder.

From case 1 to case 3, the probability of anti-symmetrical vortex shedding increases progressively from 19.5% to 46.5% at  $z^*=4$ , indicating a gradual reduction in the influence of the free-end downwash flow with increasing boundary layer thickness; the probability decreases progressively from 84.1 to 34.5 at  $z^*=1$ , suggesting that the enhanced upwash flow, as shown in Figs. 4(a), 4(c), and 4(e), tends to change vortex shedding from anti-symmetrical to symmetri-

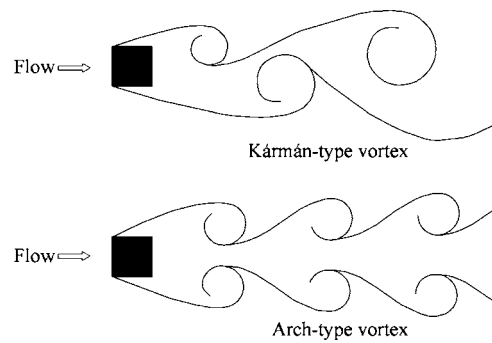


FIG. 18. Sketch of the two types of vortices formed behind the cylinder.

cal; the probability is near 64.5% in case 1 and about 50% for two other cases at  $z^*=2.5$ , that is, one type of vortices occur almost as frequently as the other.

It could be of interest to examine the spatially averaged Reynolds stresses,  $[\overline{fg}]$ , where  $f$  and  $g$  each stand for  $u$  or  $v$ , associated with anti-symmetrically and symmetrically arranged vortices, respectively, and their contributions to the overall spatially averaged Reynolds stresses. As illustrated in Fig. 19(a), data between two anti-symmetrically formed vortices of the same sign are identified with the region of anti-symmetrically arranged vortices, while those between two pairs of symmetrical vortices [Fig. 19(b)] are considered to be the region of symmetrically arranged vortices. The two

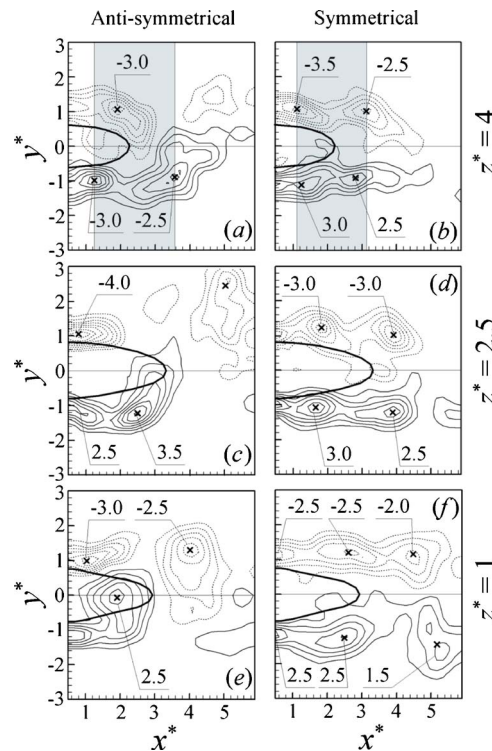


FIG. 19. Instantaneous  $\omega_z^*$  contours (contour increment=0.5) of anti-symmetrically arranged vortices (left column) and symmetrically arranged vortices (right column) for case 1. Vortex center is denoted by “×.” The shaded areas in (a-b) illustrate the part of the data used to calculate the contribution to Reynolds stresses from anti-symmetrically arranged vortices (a) or symmetrically arranged vortices (b).

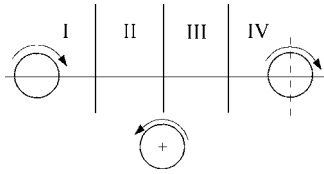


FIG. 20. Definition of antisymmetrical and symmetrical vortex shedding.

sets of data are then averaged separately to produce the spatially averaged Reynolds stresses over the detected regions.

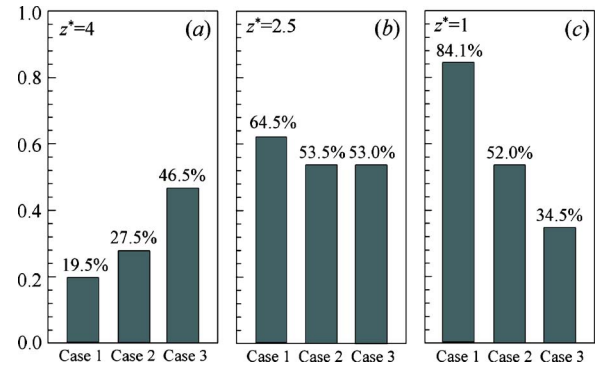
Table II lists  $[\overline{fg}]_{T1}/[\overline{fg}]_{T2}$  and  $[\overline{fg}]$ . In general,  $[\overline{u^2}]_{T1}/[\overline{u^2}]_{T2}$  is between 1.06 and 1.14, displaying little dependence on the spanwise position, that is, antisymmetrically arranged vortices contribute 6%–14% more to  $[\overline{u^2}]$  than symmetrically arranged vortices. However,  $[\overline{v^2}]_{T1}/[\overline{v^2}]_{T2}$  and  $[\overline{uv}]_{T1}/[\overline{uv}]_{T2}$  are markedly larger than unity, which is more evident for  $[\overline{v^2}]_{T1}/[\overline{v^2}]_{T2}$ . Sakamoto and Arie<sup>7</sup> suggested that the velocity fluctuation associated with antisymmetric vortex shedding was greater than that associated with symmetrical shedding. This is reasonable since antisymmetrically arranged vortices are inclined to reinforce each other in the lateral motion, thus resulting in larger  $\overline{v^2}$  and hence  $\overline{uv}$  than symmetrically arranged vortices.<sup>27,34</sup>

Following Bisset *et al.*,<sup>34</sup> the contributions,  $\alpha[\overline{fg}]_{T1}/[\overline{fg}]$  and  $\beta[\overline{fg}]_{T1}/[\overline{fg}]$ , corresponding to antisymmetrically and symmetrically arranged vortices, to  $[\overline{fg}]$  are calculated and presented in Fig. 22, where  $\alpha$  and  $\beta$  are the weighting factors, given by the probabilities (Fig. 21) of antisymmetrically and symmetrically arranged vortices, respectively. It has been verified that the sum (not shown here) of the two contributions, viz.,

$$\alpha[\overline{fg}]_{T1} + \beta[\overline{fg}]_{T2}, \quad (5)$$

is quite representative to  $[\overline{fg}]$ , with a maximal discrepancy of 8%.

Figure 22 shows that  $\alpha[\overline{fg}]_{T1}/[\overline{fg}]$  in case 1 is smallest at  $z^*=4$ , but grows remarkably at  $z^*=2.5$  and even greater at  $z^*=1$ ; the dependence of  $\beta[\overline{fg}]_{T1}/[\overline{fg}]$  on  $z^*$  is simply opposite. The observation is linked to the probabilities of occurrence for the two types of vortices. In case 1, the upwash flow effect is limited to the region close to the wall [Fig. 4(a)] because of a thin boundary layer; the flow near the free

FIG. 21. Probability of antisymmetrical vortices shedding. (a)  $z^*=4$ ; (b)  $z^*=2.5$ ; (c)  $z^*=1$ .

end is dominated by the downwash free-end shear layer, which favors the formation of symmetric vortex shedding,<sup>6,25</sup> resulting in a probability of more than 80% at  $z^*=4$  [Fig. 21(a)] and hence a predominant contribution to  $[\overline{fg}]$ . The effect of the free-end shear layer withers towards the wall, leading to the probability of antisymmetric vortex shedding growing from 19.5% at  $z^*=4$  to 84.1% at  $z^*=1$ . Consequently, the corresponding contribution to  $[\overline{fg}]$  increases greatly from  $z^*=4$  to  $z^*=1$ .

With the boundary layer condition changing from case 1 to case 3, as discussed in Sec. IV A, the time-averaged Reynolds stresses increase in magnitude near the free end but decrease near the wall. The same is observed for the spatially averaged Reynolds stresses (Table II). The thickening boundary layer enhances the upwash flow [Figs. 4(a), 4(c), and 4(e)], which encourages the formation of symmetric vortex shedding, similarly to the downwash free-end shear flow. The probability for antisymmetrically arranged vortices to occur declines from 84.1% to 34.5% at  $z^*=1$  [Fig. 21(c)]. As a result,  $\alpha[\overline{fg}]_{T1}/[\overline{fg}]$  diminishes, while  $\beta[\overline{fg}]_{T1}/[\overline{fg}]$  grows (Fig 22). Furthermore, since antisymmetrically arranged vortices produce more Reynolds stresses than symmetrically arranged ones,  $[\overline{fg}]$  displays the trend of decrease from case 1 to case 3 at  $z^*=1$  (Table II). On the other hand, the downwash free-end shear layer impairs under the influence of the enhanced upwash flow [Figs. 4(a), 4(c), and 4(e)]. Accordingly, antisymmetrical vortices increase from 19.5% to

TABLE II. Overall spatially averaged Reynolds stresses  $[\overline{fg}]$  and  $[\overline{fg}]_{T1}/[\overline{fg}]_{T2}$ .

		Case 1		Case 2		Case 3	
		$[\overline{fg}]_{T1}/[\overline{fg}]_{T2}$	$[\overline{fg}]$	$[\overline{fg}]_{T1}/[\overline{fg}]_{T2}$	$[\overline{fg}]$	$[\overline{fg}]_{T1}/[\overline{fg}]_{T2}$	$[\overline{fg}]$
$z^*=4$	$[\overline{u^2}]$	1.14	0.044	1.11	0.049	1.09	0.057
	$[\overline{v^2}]$	2.06	0.040	1.70	0.044	1.69	0.050
	$[\overline{uv}]$	1.67	0.0053	1.42	0.0068	1.58	0.0083
$z^*=2.5$	$[\overline{u^2}]$	1.10	0.051	1.08	0.053	1.08	0.052
	$[\overline{v^2}]$	1.86	0.061	1.54	0.052	1.63	0.052
	$[\overline{uv}]$	1.60	0.0068	1.37	0.0068	1.38	0.007
$z^*=1$	$[\overline{u^2}]$	1.13	0.058	1.13	0.053	1.06	0.050
	$[\overline{v^2}]$	1.79	0.054	1.42	0.050	1.51	0.049
	$[\overline{uv}]$	1.21	0.007	1.23	0.0058	1.36	0.0055

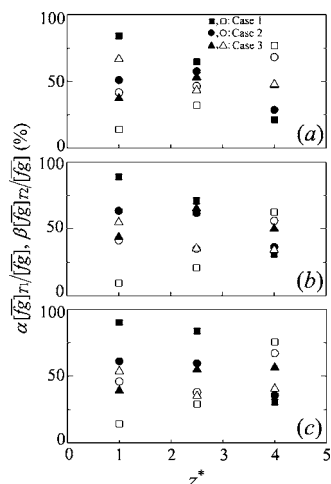


FIG. 22. Contributions to specially averaged Reynolds stresses from anti-symmetrical vortices  $\overline{[fg]}_{T1}/\overline{[fg]}$  (solid symbol) and symmetrical vortices  $\overline{[fg]}_{T1}/\overline{[fg]}$  (open symbol): (a)  $f=g=u$ ; (b)  $f=g=v$ ; (c)  $f=u$ ,  $g=v$ .

46.5% at  $z^*=4$  [Fig. 21(a)], leading to the increased  $\alpha\overline{[fg]}_{T1}/\overline{[fg]}$  and decreased  $\beta\overline{[fg]}_{T1}/\overline{[fg]}$  from case 1 to case 3 (Fig. 22). This increase in antisymmetrical vortices is responsible for increasing  $\overline{[fg]}$  at  $z^*=4$ , as evident in Table II.

## V. CONCLUSIONS

Interaction between a boundary layer and a wall-mounted finite-length square-cylinder wake is experimentally investigated. Three different initial boundary layer conditions are examined, their momentum thickness being  $0.07d$ ,  $0.13d$ , and  $0.245d$ , respectively. Following conclusions may be drawn from the investigation:

(i) The flow around the finite-length cylinder is highly 3D, largely consisting of three vortical structures, i.e., the tip vortex, the spanwise vortex and the base vortex. While the tip vortex is clearly connected to the downwash shear layer from the free end, the base vortex induces an upwash flow from the junction of the wall and the cylinder base. Under the effect of the tip and the base vortices, the longitudinal size of the reverse flow region exceeds twice of that in the wake of a 2D cylinder.

(ii) It has been found that the boundary layer conditions have a profound effect on the flow around the finite-length cylinder, not only near the wall but also well beyond the near-wall region (outside the boundary layer). With increasing boundary layer thickness, the base vortex is enhanced. So is the upwash flow, which acts to weaken the tip vortex and the downwash of the free-end shear layers. As a result, the reverse flow region retreats significantly near the wall but grows near the free end. The mean flow also differs in  $\overline{U^*}$ ,  $\overline{V^*}$ , and  $\overline{W^*}$ . At the same time, the Reynolds stresses, i.e.,  $\overline{u^{*2}}$ ,  $\overline{v^{*2}}$ , and  $\overline{u^*v^*}$ , increase in magnitude near the free end but decrease near the wall.

(iii) The boundary layer conditions have a great influence upon the occurrence of antisymmetrically and symmetrically arranged vortices. In case 1, where the boundary layer is thin and the upwash flow is limited, symmetrically arranged vortices overwhelm antisymmetrically arranged

ones near the free end due to the predominant downwash shear layers, which promote symmetric vortex shedding. It is the other way around near the wall. With the thickening boundary layer, the enhanced upwash flow weakens the downwash shear layers. As a result, the probability of anti-symmetrical vortices increases near the free end but drops rapidly near the wall. Since this type of vortices produce more Reynolds stresses than symmetrically arranged ones, the overall spatially averaged Reynolds stresses,  $\overline{[u^{*2}]}$ ,  $\overline{[v^{*2}]}$ , and  $\overline{[u^*v^*]}$ , increase in magnitude near the free end but decrease near the wall.

The flow behind a wall-mounted finite-length cylinder has been experimentally documented in terms of the dependence on the boundary layer thickness of the reverse flow region, sectional streamlines and vorticity contours in the  $x$ - $z$  plane, as well as the distribution of  $\overline{U^*}$ ,  $\overline{V^*}$ ,  $\overline{W^*}$ ,  $\overline{u^{*2}}$ ,  $\overline{v^{*2}}$ ,  $\overline{w^{*2}}$ ,  $\overline{u^*v^*}$ , and  $\overline{u^*w^*}$ , which is important for the future numerical modeling of this flow.

## ACKNOWLEDGMENTS

Y.Z. wishes to acknowledge support given to him by the Research Grants Council of the Government of the HKSAR through Grant No. PolyU B-Q862 and by the Central Research Grant of The Hong Kong Polytechnic University through Grant No. G-YD69.

- <sup>1</sup>A. Roshko, "Perspectives on bluff body aerodynamics," *J. Wind. Eng. Ind. Aerodyn.* **49**, 561 (1993).
- <sup>2</sup>C. H. K. Williamson, "Vortex dynamics in the cylinder wake," *Annu. Rev. Fluid Mech.* **28**, 477 (1996).
- <sup>3</sup>M. Matsumoto, "Vortex shedding of bluff bodies: a review," *J. Fluids Struct.* **13**, 791 (1999).
- <sup>4</sup>F. Etzold and H. Fiedler, "The near-wake structure of a cantilevered cylinder in a cross-flow," *Z. Flugwiss.* **24**, 77 (1976).
- <sup>5</sup>T. Kawamura, M. Hiwada, T. Hibino, I. Mabuchi, and M. Kumada, "Flow around a finite circular cylinder on a flat plate," *Bull. JSME* **27**, 2142 (1984).
- <sup>6</sup>S. Okamoto and Y. Sunabashiri, "Vortex shedding from a circular cylinder of finite length placed on a ground plane," *J. Fluids Eng.* **114**, 512 (1992).
- <sup>7</sup>H. Sakamoto and M. Arie, "Vortex shedding from a rectangular prism and a circular cylinder placed vertically in a turbulent boundary layer," *J. Fluid Mech.* **126**, 147 (1983).
- <sup>8</sup>C. W. Park and S. J. Lee, "Free-end effects on the near wake flow structure behind a finite circular cylinder," *J. Wind. Eng. Ind. Aerodyn.* **88**, 231 (2000).
- <sup>9</sup>J. C. R. Hunt, C. J. Abell, J. A. Peterka, and H. Woo, "Kinematical studies of the flows around free of surface-mounted obstacles; applying topology to flow visualization," *J. Fluid Mech.* **86**, 179 (1978).
- <sup>10</sup>H. J. Hussein and R. J. Martinuzzi, "Energy balance of turbulent flow around a surface mounted cube placed in a channel," *Phys. Fluids* **8**, 764 (1996).
- <sup>11</sup>J. Fröhlich and W. Rodi, "LES of the flow around a circular cylinder of finite height," *Int. J. Heat Fluid Flow* **25**, 537 (2004).
- <sup>12</sup>J. L. Sumner, J. L. Heseltine, and O. J. P. Dansereau, "Wake structure of a finite circular cylinder of small aspect ratio," *Exp. Fluids* **37**, 720 (2004).
- <sup>13</sup>H. F. Wang, Y. Zhou, and C. K. Chan, "Flow around a finite length square prism," in *Proceedings of the 4th European & African Conference on Wind Engineering* (Institute of Theoretical and Applied Mechanics, Academy of Sciences of the Czech Republic, Prague), July 2005, Paper No. 314.
- <sup>14</sup>I. Wygnanski, B. Champagne, and B. Marasli, "On the large-scale structures in two-dimensional, small-deficit, turbulent wakes," *J. Fluid Mech.* **168**, 31 (1986).
- <sup>15</sup>Y. Zhou and R. A. Antonia, "Effect of initial conditions on structures in a turbulent near-wake," *AIAA J.* **32**, 1207 (1994).
- <sup>16</sup>Y. Zhou and R. A. Antonia, "Memory effects in a turbulent plane wake,"

- Exp. Fluids **19**, 112 (1995).
- <sup>17</sup>A. Ayoub and K. Karamcheti, "An experiment on the flow past a finite circular cylinder at high subcritical and supercritical Reynolds number," *J. Fluid Mech.* **118**, 1 (1982).
- <sup>18</sup>C. W. Park and S. J. Lee, "Flow structure around a finite circular cylinder embedded in various atmospheric boundary layers," *Fluid Dyn. Res.* **30**, 197 (2002).
- <sup>19</sup>Z. J. Wang, Y. Zhou, J. F. Huang, and Y. L. Xu, "Fluid dynamics around an inclined cylinder with running water rivulets," *J. Fluids Struct.* **21**, 49 (2005).
- <sup>20</sup>R. L. Simpson, "Junction flow," *Annu. Rev. Fluid Mech.* **33**, 415 (2001).
- <sup>21</sup>D. A. Lyn, S. Einav, W. Rodi, and J. H. Park, "A laser-Doppler velocimetry study of ensemble-averaged characteristics of the turbulent near wake of square cylinder," *J. Fluid Mech.* **304**, 285 (1995).
- <sup>22</sup>Y. Zhou and R. A. Antonia, "Critical points in a turbulent near wake," *J. Fluid Mech.* **275**, 59 (1994).
- <sup>23</sup>A. K. Saha, K. Muralidhar, and G. Biswas, "Experimental study of flow past a square cylinder at high Reynolds numbers," *Exp. Fluids* **29**, 553 (2000).
- <sup>24</sup>S. Bloor, "The transition to turbulence in the wake of a circular cylinder," *J. Fluid Mech.* **19**, 290 (1964).
- <sup>25</sup>D. Farivar, "Turbulent uniform flow around cylinders of finite length," *AIAA J.* **19**, 275 (1981).
- <sup>26</sup>A. K. M. F. Hussain and M. Hayakawa, "Eduction of large-scale organized structures in a turbulent plane wake," *J. Fluid Mech.* **180**, 193 (1987).
- <sup>27</sup>Y. Zhou and R. A. Antonia, "A study of turbulent vortices in the near wake of a cylinder," *J. Fluid Mech.* **253**, 643 (1993).
- <sup>28</sup>A. E. Perry and M. S. Chong, "A description of eddying motions and flow patterns using critical-point concepts," *Annu. Rev. Fluid Mech.* **19**, 125 (1987).
- <sup>29</sup>M. Kiya and M. Matsumura, "Incoherent turbulence structure in the near wake of a normal plate," *J. Fluid Mech.* **190**, 343 (1988).
- <sup>30</sup>Y. Zhou, H. J. Zhang, and M. W. Yiu, "The turbulent wake of two side-by-side circular cylinders," *J. Fluid Mech.* **458**, 303 (2002).
- <sup>31</sup>J. C. R. Hunt, A. A. Wray, and P. Moin, "Eddies, stream and convergence zones in turbulent flow," Center for Turbulence Research Report No. CTR-S88, p. 193 (1988).
- <sup>32</sup>Y. Dubief and F. Delcayre, "On the coherent-vortex identification in turbulent," *J. Turbul.* **1**, 011 (2000).
- <sup>33</sup>J. Jeong and F. Hussain, "On the identification of a vortex," *J. Fluid Mech.* **285**, 69 (1995).
- <sup>34</sup>D. K. Bisset, R. A. Antonia, L. W. B. Browne, "Spatial organization of large structures in the turbulent far wake of a cylinder," *J. Fluid Mech.* **218**, 439 (1990).